

## Nanophotonic supercontinuum-based mid-infrared dual-comb spectroscopy: supplement

HAIRUN GUO,<sup>1,5,†</sup>  WENLE WENG,<sup>1,†</sup> JUNQIU LIU,<sup>1,†</sup> FAN YANG,<sup>2</sup>  WOLFGANG HÄNSEL,<sup>3</sup> CAMILLE SOPHIE BRÈS,<sup>4</sup> LUC THÉVENAZ,<sup>2</sup>  RONALD HOLZWARTH,<sup>3</sup> AND TOBIAS J. KIPPENBERG<sup>1,\*</sup>

<sup>1</sup>Laboratory of Photonics and Quantum Measurements (LPQM), Swiss Federal Institute of Technology Lausanne (EPFL), CH-1015 Lausanne, Switzerland

<sup>2</sup>Group for Fiber Optics (GFO), Swiss Federal Institute of Technology Lausanne (EPFL), CH-1015 Lausanne, Switzerland

<sup>3</sup>Menlo Systems GmbH, 82152 Martinsried, Germany

<sup>4</sup>Photonic Systems Laboratory (PHOSL), Swiss Federal Institute of Technology Lausanne (EPFL), CH-1015 Lausanne, Switzerland

<sup>5</sup>Key laboratory of Specialty Fiber Optics and Optical Access Networks, Joint International Research Laboratory of Specialty Fiber Optics and Advanced Communication, Shanghai Institute for Advanced Communication and Data Science, Shanghai University, Shanghai 200443, China

\*Corresponding author: [tobias.kippenberg@epfl.ch](mailto:tobias.kippenberg@epfl.ch)

†These authors contributed equally to the work.

---

This supplement published with The Optical Society on 8 September 2020 by The Authors under the terms of the [Creative Commons Attribution 4.0 License](https://creativecommons.org/licenses/by/4.0/) in the format provided by the authors and unedited. Further distribution of this work must maintain attribution to the author(s) and the published article's title, journal citation, and DOI.

Supplement DOI: <https://doi.org/10.6084/m9.figshare.12730406>

Parent Article DOI: <https://doi.org/10.1364/OPTICA.396542>

# Supplement to “Nanophotonic supercontinuum based mid-infrared dual-comb spectroscopy”

HAIRUN GUO<sup>1,5,†</sup>, WENLE WENG<sup>1,†</sup>, JUNQIU LIU<sup>1,†</sup>, FAN YANG<sup>2</sup>,  
WOLFGANG HÄNSEL<sup>3</sup>, CAMILLE SOPHIE BRÈS<sup>4</sup>, LUC THÉVENAZ<sup>2</sup>,  
RONALD HOLZWARTH<sup>3</sup>, AND TOBIAS J. KIPPENBERG<sup>1,\*</sup>

<sup>1</sup>Laboratory of Photonics and Quantum Measurements (LPQM), Swiss Federal Institute of Technology Lausanne (EPFL), CH-1015 Lausanne, Switzerland

<sup>2</sup>Group for Fiber Optics (GFO), Swiss Federal Institute of Technology Lausanne (EPFL), CH-1015 Lausanne, Switzerland

<sup>3</sup>Menlo Systems GmbH, 82152 Martinsried, Germany

<sup>4</sup>Photonic Systems Laboratory (PHOSL), Swiss Federal Institute of Technology Lausanne (EPFL), CH-1015 Lausanne, Switzerland

<sup>5</sup>Key laboratory of Specialty Fiber Optics and Optical Access Networks, Joint International Research Laboratory of Specialty Fiber Optics and Advanced Communication, Shanghai Institute for Advanced Communication and Data Science, Shanghai University, Shanghai 200443, China

\*Corresponding author: tobias.kippenberg@epfl.ch

†These authors contribute equally to the work.

Compiled July 21, 2020

## 1. DISPERSION LANDSCAPE UNDERLYING SUPERCONTINUUM GENERATION

In theory, nonlinear wave propagating dynamics in a waveguide can be described by the following wave equation [1]: (where we only consider the spontaneous response in the cubic nonlinearity)

$$\frac{\partial \tilde{E}(\omega, \mathbf{r})}{\partial z} = -i\beta(\omega)\tilde{E}(\omega, \mathbf{r}) - i\frac{\omega\chi^{(3)}}{2cn}\mathcal{F}[E(t, \mathbf{r})^3]_{\omega} \quad (\text{S1})$$

where  $E(t, \mathbf{r})$  indicates the electric field of the light wave in the time domain ( $t$ -axis), and its amplitude spectral density is  $\tilde{E}(\omega, \mathbf{r})$  in the frequency domain ( $\omega$ -axis), namely via the Fourier transform (operator  $\mathcal{F}$ ):  $\tilde{E}(\omega, \mathbf{r}) = \int dt E(t, \mathbf{r})e^{-i\omega t} \triangleq \mathcal{F}[E(t, \mathbf{r})]_{\omega}$ ,  $\mathbf{r} = \{x, y, z\}$  indicates the space frame, and the light propagation direction in the waveguide is defined as the  $z$ -axis,  $\beta(\omega)$  indicates the propagation constant of the light wave in a waveguide, which is frequency dependent reflecting dispersive properties;  $n$  is the effective refractive index of the waveguide;  $\chi^{(3)}$  is the cubic nonlinear susceptibility of the waveguide material;  $c$  is the speed of light in vacuum. The electric-field can be further expressed as:

$$\tilde{E}(\omega, \mathbf{r}) = \tilde{B}(\omega, x, y)\tilde{A}(\omega, z) \quad (\text{S2})$$

where  $\tilde{B}$  indicates the normalized mode distribution, namely  $\iint dx dy \tilde{B}^2 = 1$ . Thus the propagation dynamics of the light field is enfolded in  $\tilde{A}$  and the Eq. S1 can be modified to: (if only

considering the nonlinear phase modulation effect, i.e. the Kerr nonlinearity)

$$\frac{\partial \tilde{A}(\omega, z)}{\partial z} = -i\beta(\omega)\tilde{A}(\omega, z) - i\frac{\omega}{c}\frac{\chi^{(3)}}{2nA_{\text{eff}}}\mathcal{F}[|A(t, z)|^2 A(t, z)]_{\omega} \quad (\text{S3})$$

where information of the mode confinement in the waveguide is reflected on the parameter of the effective mode area,  $A_{\text{eff}}$ .

We further assume that the light wave consists of a primary wave packet  $\tilde{A}_s$  (seeded by the pump wave and assumed as high-order soliton pulses, i.e. the soliton number  $N > 1$ ) and a nonlocal small wave  $\tilde{\sigma}$  (i.e. the dispersive wave), namely:

$$\tilde{A}(\omega > 0, z) = \tilde{A}_s(\Omega, z)e^{-i\beta_s z} + \tilde{\sigma}e^{-i\beta(\omega_d)z} \quad (\text{S4})$$

where  $\Omega = \omega - \omega_s$  defines a relative frequency frame with respect to the pumping frequency  $\omega_s$ ,  $\beta_s(\Omega)$  indicates the phase constant of the soliton, which is dispersionless, i.e.:

$$\beta_s(\Omega) = \beta(\omega_s) + \Omega\beta^{(1)}(\omega_s) + q \quad (\text{S5})$$

where  $\beta^{(m)}(\omega) = \frac{\partial^m}{\partial \omega^m}\beta(\omega)$  indicates the  $m$ -th order of dispersion with respect to  $\omega_s$ ,  $v_g = 1/\beta^{(1)}(\omega)$  is also known as the group velocity of the soliton,  $q$  stands for the nonlinear induced phase constant, which in our case is small valued and neglected,  $\omega_d$  indicates the central frequency of the small wave, which is non-local with respect to the soliton (i.e.  $\omega_d \neq \omega_s$ ).

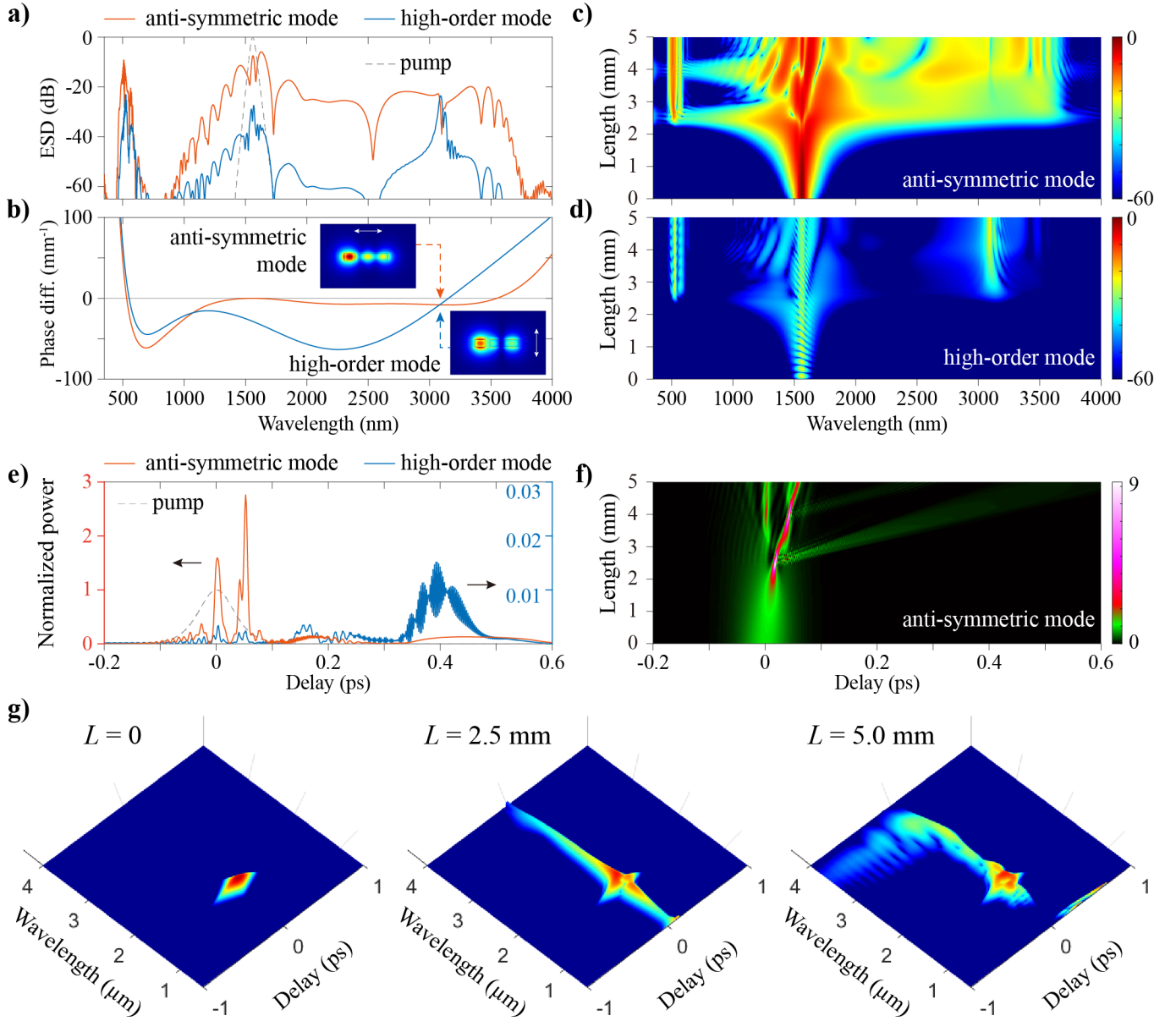


**Fig. S1. Supercontinuum simulation in dual-core waveguides.** (a) Simulated output spectrum in both the anti-symmetric mode and the orthogonal polarized high-order mode. The peak power of the pump pulses is set 4.5 kW, pulse duration 75 fs, pump wavelength 1560 nm, and  $\kappa = 1 \text{ mm}^{-1}$ . (b) Dispersion profile  $\Delta\beta_i$  of the two modes, where phase matching is found at the wavelength of 3100 nm. Insets are the spatial mode distribution of the two coupled modes at 3100 nm. (c, d) Wave spectral evolution in the two modes, over the propagation distance. (e) Temporal profile of the output wave in the two modes. The wave power is normalized to the peak power of the input pump pulses. (f) Wave temporal evolution in the anti-symmetric mode, over the propagation distance. (g) Cross-correlation frequency resolved optical gating (XFROG) traces of the wave in the anti-symmetric mode, at different propagation positions (lengths).

From Eq. S4 in Eq. S3, we derive the following equations:

$$\frac{\partial \tilde{A}_s}{\partial z} = -i\Delta\beta(\omega)\tilde{A}_s - i\frac{\omega}{c}\frac{3\chi^{(3)}}{8nA_{\text{eff}}}\mathcal{F}[|A_s|^2 A_s]_{\Omega} \quad (\text{S6})$$

$$\tilde{\sigma} \approx \tilde{A}_s e^{i\Delta\beta(\omega_d)z} \quad (\text{S7})$$

where  $\tilde{A}_s = \mathcal{F}[A_s]_{\Omega}$ . Equation S6 is written in the frequency domain ( $\Omega$ -axis), and its form in the time domain is the well-known nonlinear Schrödinger equation with full dispersion ( $\Delta\beta(\omega) = \beta(\omega) - \beta_s = \sum_{m \geq 2} \frac{\beta^{(m)}}{m!} \Omega^m$ , also called a dispersion landscape over a large spectral range). In particular, with anomalous group velocity dispersion (GVD), i.e.  $\beta^{(2)} < 0$ , high-order

soliton pulses will feature spectral broadening during the propagation in the waveguide. Equation S7 is derived in the condition when  $\Delta\beta(\omega_d) \rightarrow 0$ , which indicates the phase matching between the pump wave and the dispersive wave. In this condition, the dispersive wave generation is dominated by linear coupling to the spectral sideband of the pump wave, while the nonlinear effect is neglected. Hence, the power of the dispersive wave is dependent on the sideband power of the pump, and the latter is further determined by the soliton spectral broadening by the nonlinear self-phase modulation (SPM) effect. More generally, the generation of a broadband dispersive wave requires that  $\Delta\beta(\omega) \rightarrow 0$ .

In addition, the profile of  $\Delta\beta(\omega)$  also represent the full dis-

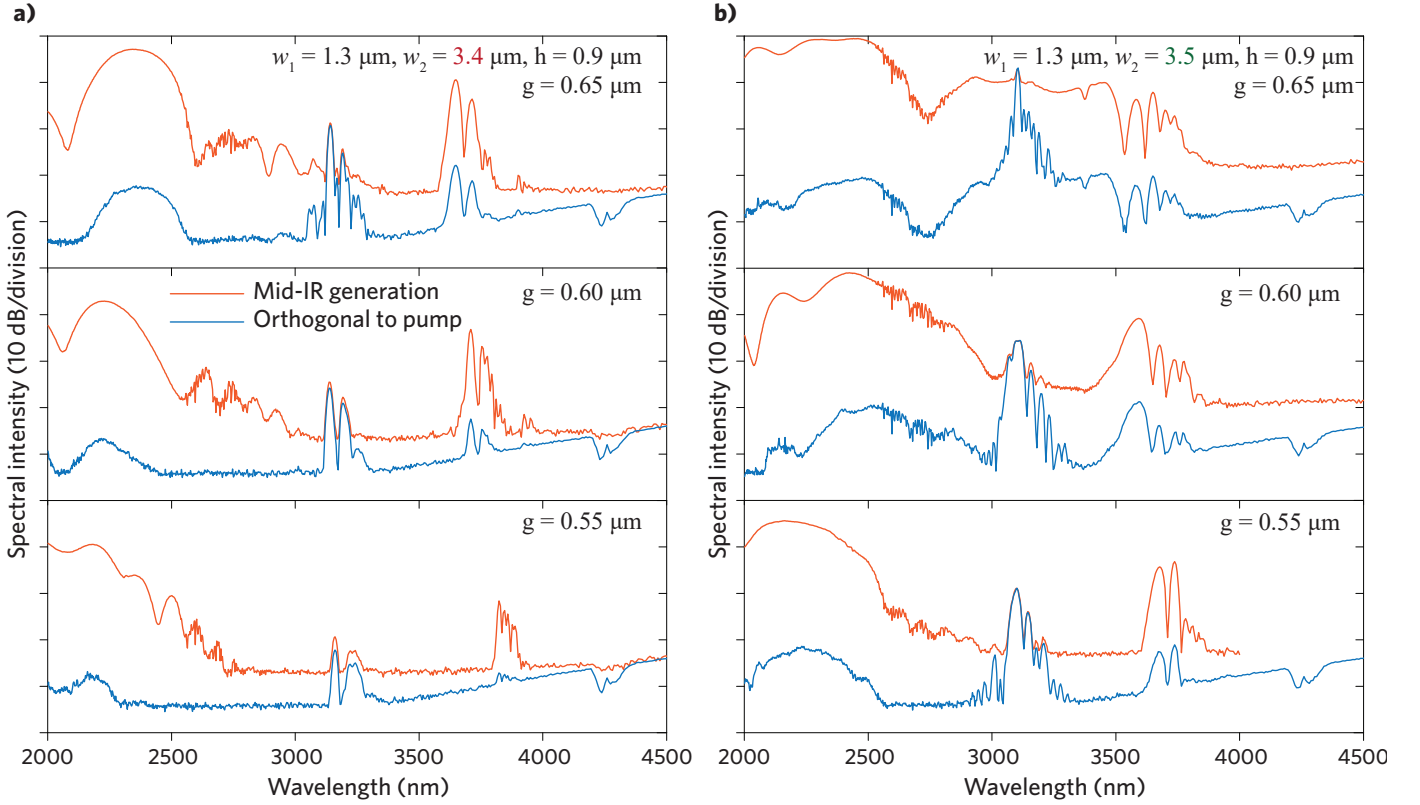


**Fig. S2. Engineered mid-IR wave generation in hybrid dual-core waveguides.** (a) A panel of experimentally acquired spectra in three dual-core  $\text{Si}_3\text{N}_4$  nano-photonic waveguides, in which the gap  $g$  parameter is tuned while other parameters are fixed as:  $w_1 = 1.3 \mu\text{m}$ ,  $w_2 = 3.4 \mu\text{m}$  and  $h = 0.9 \mu\text{m}$ . (b) A similar panel of spectra in the second set of waveguides where only the parameter  $w_2 = 3.5 \mu\text{m}$  is different to that in (a). Note: the pumping source is horizontally polarized and the overall spectrum is measured and shown as the red curve, while the blue curve represents the optical spectrum measured after a linear polarizer that is set orthogonal to the pump.

persion of the waveguide that will counterbalance the nonlinear SPM, and the condition for reaching the maximum soliton spectral broadening is also  $\Delta\beta(\omega) \rightarrow 0$ .

Therefore,  $\Delta\beta(\omega)$  works as a “spectral barrier” that impacts both the level of soliton spectral broadening and consequently the power of dispersive waves. In this work, the region  $\omega \in [\omega_s, \omega_d]$  is of highest interest. Our design purpose is exactly to reduce the barrier within this region such as to obtain a broadband and flat supercontinuum bridging the near-IR pump wave and the mid-IR dispersive wave.

## 2. SUPERCONTINUUM SIMULATION IN DUAL-CORE WAVEGUIDES

The supercontinuum simulation is based on the nonlinear Schrödinger equation, i.e. Eq. S6. In addition, to include also the effect of mode coupling to a high-order mode, we applied coupled wave equations, namely:

$$\frac{\partial \tilde{A}_1}{\partial z} = -i\Delta\beta_1(\omega)\tilde{A}_1 - ik\tilde{A}_2 - i\frac{\omega}{c} \frac{3\chi^{(3)}}{8nA_{\text{eff}}} \mathcal{F}[|A_1|^2 A_1]_{\Omega} \quad (\text{S8})$$

$$\frac{\partial \tilde{A}_2}{\partial z} = -i\Delta\beta_2(\omega)\tilde{A}_2 - ik\tilde{A}_1 \quad (\text{S9})$$

where  $\tilde{A}_1$  indicates the wave spectral amplitude based in the anti-symmetric mode of the dual-core waveguide, and  $\tilde{A}_2$  is the wave in the high-order mode,  $\Delta\beta_j = \beta_j(\omega) - \beta_s$  ( $j = 1, 2$ ) is the full dispersion profile of the two modes,  $\beta_j(\omega)$  is the

mode propagation constant,  $\kappa$  indicates the strength of the mode coupling. The nonlinear effects on the high-order mode are neglected, due to the fact that the coupling to an orthogonal polarized high-order mode is narrow-band and is low-efficient, i.e.  $\kappa \ll \Delta\beta_j$ .

The simulated waveguide geometry is:  $w_1 = 1.3 \mu\text{m}$ ,  $w_2 = 3.4 \mu\text{m}$ ,  $h = 0.85 \mu\text{m}$ , and  $g = 0.8 \mu\text{m}$ , in which the propagation phase constant of all supported modes is calculated via a finite element method. In this way, the dispersion profile of the anti-symmetric mode and the high-order mode is extracted. In simulations, we set the peak power of the pump pulses to be 4.5 kW, pulse duration 75 fs. The pump pulses are launched to the anti-symmetric mode, at the wavelength of 1560 nm, and the overall propagation length is 5 mm. The coupling strength is  $\kappa = 1 \text{ mm}^{-1}$ .

The simulation result is shown in Fig. S1. The output spectral envelope in both the anti-symmetric mode and the high-order mode shows a high level of agreement with the experiment (cf. Fig. S1(a) for the simulation and Fig. 2(d) in the main article for the experimental result). The corresponding dispersion profile of the two modes are shown in Fig. S1(b), and a phase matching is found at the wavelength of 3100 nm, indicating the generation of a narrow-band wave in the high-order mode. Interestingly, this high-order mode is a vertically polarized TM mode, while the pump wave and the generated wave in the anti-symmetric mode are horizontally polarized. In reality, the potential of mode coupling among different polarization directions is prob-

ably due to the existence of non-orthogonal boundaries in the waveguide, e.g. the cross section of waveguide cores are not perfect rectangular (cf. Fig. 1).

Moreover, the simulation unveils details of the supercontinuum process during the wave propagation in the waveguide, including the wave evolution in both the frequency and the time domain, the output wave temporal profile, and the frequency resolved optical gating (FROG) traces. In the spectral evolution diagram, see Fig. S1(c, d), the wave spectral broadening is initiated at the distance of 2.5 mm. Afterwards, the flat supercontinuum was implemented in the anti-symmetric mode, and a narrow-band wave in the high-order mode is increasingly generated at the phase matching wavelength of 3100 nm. At other wavelengths, namely the pump wavelength and the visible wavelength, the wave in the high-order mode is periodically presented, which is a typical phenomenon of light coupling in the presence of phase mismatch. In the time domain, the supercontinuum process is along with the temporal soliton self-compression, which leads to the generation of high-intensity and few-cycle soliton pulses, see Fig. S1(e). The temporal evolution diagram shows that the pump wave after the first compression point is split into two few-cycle soliton pulses that can preserve themselves during the propagation, see Fig. S1(f). The temporal interference of solitons also gives rise to a periodic waveform in the supercontinuum. In addition, dispersive waves are observed temporally emitted from the soliton, due to their different group velocity to solitons, which reflects the nature of the Cherenkov radiation [2].

We also simulated the frequency resolved optical gating (FROG) traces of the wave in the anti-symmetric mode, at different propagation positions. These traces are based on the cross-correlation between the wave temporal profile and an referenced optical pulse serving as the gate signal, and can reveal the spatial-temporal diagram of the supercontinuum. In the dual-core waveguide, FROG traces confirm that a large portion of the pump energy is converted to the mid-IR range, forming a broadband supercontinuum, see Fig. S1(g).

### 3. ENGINEERED MID-IR CONTINUUM VIA GEOMETRY CONTROL

Here we present the effect of engineering the mid-IR spectral structure by means of tuning the waveguide geometry, see Fig. S2, in which the pumping condition was kept unchanged (pulse energy  $\sim 1$  nJ) and the waveguide length is always 5 mm. Generally, we find that the mid-IR continuum is built up by two parts: the long wavelength edge is raised by the mid-IR dispersive wave that is determined by the phase matching; the moderate-wavelength part (in between the dispersive wave and the edge of the broadened soliton sideband) that is by the mode hybridization where the dispersion landscape is changed such that the overall phase mismatch is reduced. As a result, it can be observed that by decreasing the gap distance between the two  $\text{Si}_3\text{N}_4$  cores, the mid-IR dispersive wave is slightly shifted to longer wavelengths, and in the meantime, the effect of mode hybridization on raising the moderate-wavelength part is reduced. The latter is counter-intuitive as a closer gap usually means stronger mode coupling effect. However, this increased mode coupling would also involve a large wavelength span such that the relative phase-change over wavelength (which is directly linked to the induced group velocity dispersion) is reduced. The orthogonal polarized beam, by mode coupling to a higher-order hybrid mode, is found almost independent on the change of the

waveguide geometry, i.e. the change in the gap distance as well as in the width of the wide waveguide core.

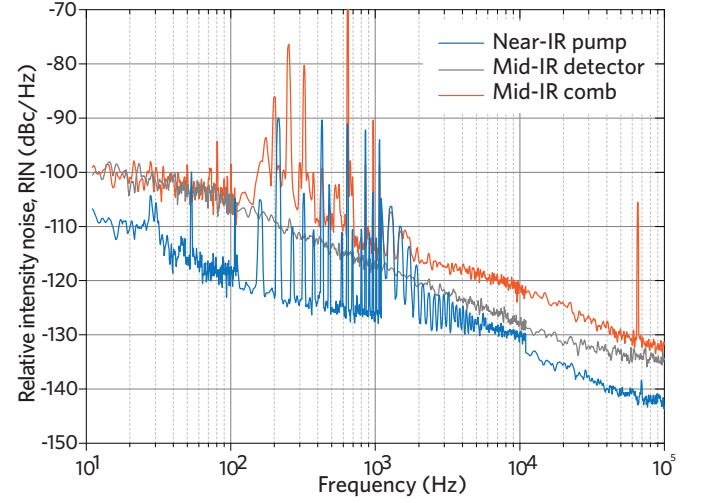


**Fig. S3. Relative intensity noise spectra of the dual-comb system.** Comparison between the measured RIN spectra of the amplified near-IR pump laser and the mid-IR emission from the waveguide shows that the RIN of the mid-IR light is approximately 10 dB higher than that of the pump source at frequency range between 100 Hz and 100 kHz. At relatively low frequencies the RIN measurement of the mid-IR light is limited by the noise floor of the mid-IR photodetector, which is also presented.

### 4. LOCKING OF FIBER-LASER FREQUENCY COMBS

In experiments, the two comb sources are fully stabilized both in the carrier-envelope offset frequency ( $f_{\text{CEO}}$ ) and in the repetition rate ( $f_{\text{rep}}$ ). The latter is implemented by having one comb mode in the C-band optically locked to a stable continuous wave (CW) reference laser (at the frequency  $f_{\text{CW}}$ ), resulting in a beat signal  $\nu_{\text{beat}}$ .  $f_{\text{CEO}}$  and  $\nu_{\text{beat}}$  are locked to have the same radio frequency, i.e.  $f_{\text{CEO}} + \nu_{\text{beat}} = 0$ . Therefore the repetition rate of the frequency comb can be easily derived as:

$$f_{\text{CW}} = f_{\text{CEO}} + Nf_{\text{rep}} + \nu_{\text{beat}}, \quad (\text{S10})$$

$$f_{\text{rep}} = \frac{f_{\text{CW}}}{N} \quad (\text{S11})$$

where  $N$  is the index of the locked comb mode.

Sharing the same reference laser, the two combs are mutually locked as well. The index of the locked mode is different by one in between the two combs, namely the second comb has  $f_{\text{rep},2} = \frac{f_{\text{CW}}}{N+1}$ . Therefore the difference in the repetition rate is:

$$\Delta f_{\text{rep}} = \frac{f_{\text{CW}}}{N(N+1)} \quad (\text{S12})$$

which is usually small valued compared with the repetition rate, such that the dual-comb configuration can cover a large span of optical window. In our work, we have  $f_{\text{rep}} \approx 250$  MHz and  $\Delta f_{\text{rep}} \approx 320$  Hz. Therefore, the optical spectral coverage is estimated as:

$$f_{\text{rep}} \times \frac{f_{\text{rep}}/2}{\Delta f_{\text{rep}}} \approx 100 \text{ THz} \quad (\text{S13})$$

which is sufficient to cover a broadband mid-infrared spectroscopic window.

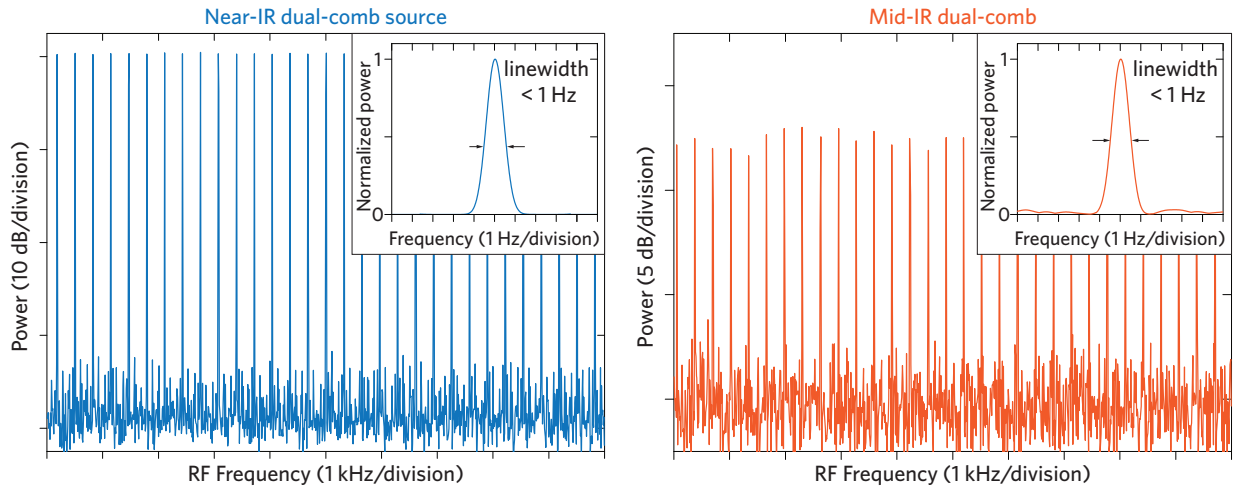


**Fig. S4. Mutual linewidths of the dual-comb system.** Measured RF spectra of the dual-comb beat signals of the near-IR pump lasers (left) and the mid-IR emissions (right). The insets show the magnified spectra of individual beat signals, which exhibit linewidths of sub-hertz level that are limited by the 1 Hz resolution bandwidth of the ESA.

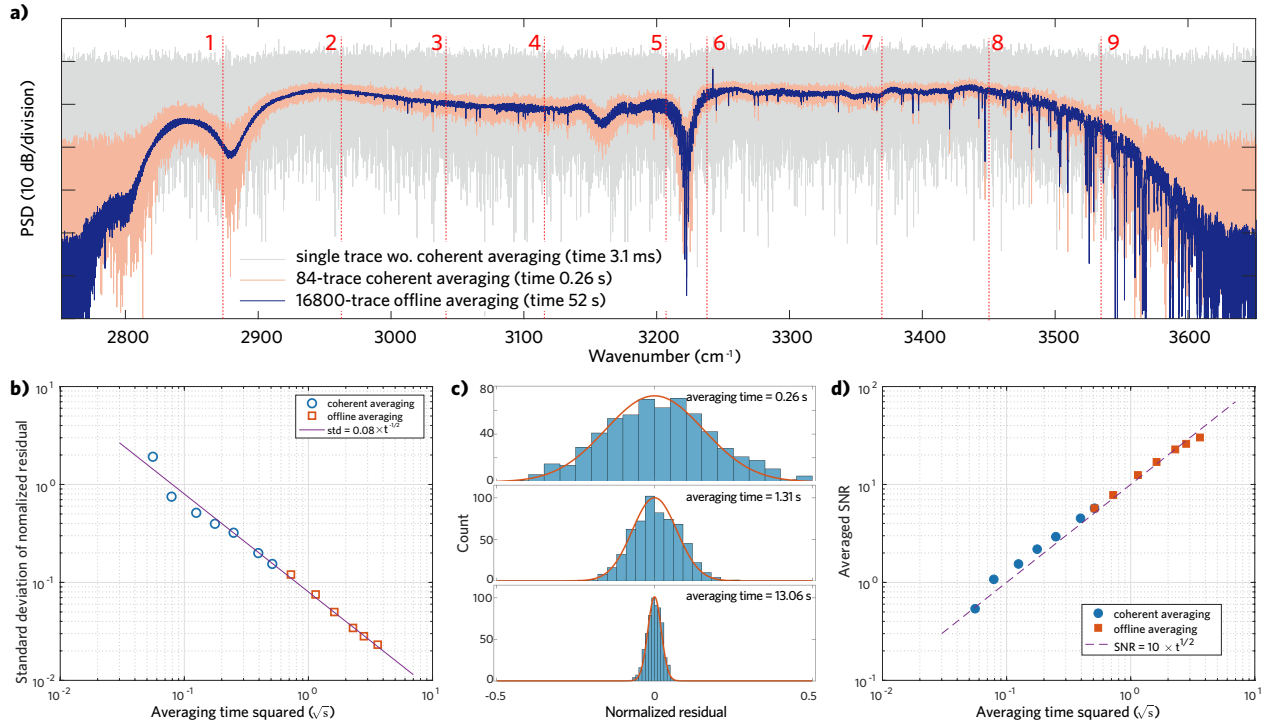


**Fig. S5. Calculation of the signal-to-noise ratio and the DCS figure of merit.** (a) Retrieved spectra of the Mid-IR dual-comb spectrometer with respect to the purged gas cell, under three averaging time, i.e. single trace without coherent averaging (3.1 ms), 84-trace realtime coherent averaging (0.26 s), and 16800-trace offline averaging (52 s). Red dash lines indicate the 9 spectral position where the optical SNR is estimated. (b) The standard deviation (std) of the normalized fitting residuals at the wavenumber  $3205\text{cm}^{-1}$ , as a function of averaging time. (c) Three histograms of the normalized fitting residuals at  $3205\text{cm}^{-1}$ , under different averaging time. Red curves indicate the Gaussian fitting of the residuals. (d) The averaged optical SNR with respect to the 9 selected spectral positions, as a function of the averaging time. The dependence of SNR on the averaging time (i.e. the normalized optical SNR) is  $10 / \sqrt{s}$ .

In addition, the beat signals ( $\nu_{\text{beat}}$ ) for the mutual optical referencing are derived in close proximity compared with the free-space section (i.e. the mode spacing of the comb) in order to keep phase drifts at a minimum. This leads to a coherence time  $> 1$  s as demonstrated in the RF spectra (cf. the following section), and at the same time enables coherent averaging for at least 84 interferograms (cf. the section of coherent averaging).

## 5. RELATIVE INTENSITY NOISE AND SIGNAL LINEWIDTH

We used an FFT analyzer to measure the Relative intensity noise (RIN) of the dual-comb system. see Fig. S3. The mid-IR RIN spectrum exhibits a level approximately 10 dB higher than that of the pump laser source. A similar deterioration of the RIN performance has been previously observed and investigated for the supercontinuum generation in fiber optics [3]. At frequen-

cies from 100 Hz to 1 kHz we observed multiple spectral peaks, which are attributed to the mechanical and acoustical vibrations in the experimental setup. In future works passive vibration cancellation and active laser intensity control can be applied to improve the RIN of the mid-IR dual-comb system.

Next we measured the RF comb spectra of the dual-comb system at both the near-IR pump branch and the mid-IR branch with an electrical spectrum analyzer (ESA). The spectra are displayed in Fig. S4. The RF beat signals show linewidths of sub-hertz level, which is limited by the minimum resolution bandwidth (RBW) of the ESA. The results show that the mutual coherence time of the mid-IR combs is at least of the order of 1 s, which potentially allows us to carry out realtime coherent averaging for a period that is significantly longer than the 0.26 s in this work, which is currently limited by the FPGA board.

## 6. AVERAGING OF INTERFEROGRAMS

Triggered by the pulse repetition rate of one of the near-IR pump lasers, the FPGA data acquisition unit can record the output voltage level of the mid-IR photodetector and continuously save up to 84 interferograms. Each interferogram trace has the length of  $\sim 3.1$  ms, corresponding to the repetition frequency difference of  $\sim 320$  Hz between the two combs, and the acquisition time for 84 interferograms is 0.26 s. The data is then read out on a computer, which in the meantime co-adds these interferograms and performs averaging to get a single averaged interferogram. We refer to this onboard averaging as realtime coherent averaging. In fact, after each 84 interferograms recorded in the FPGA, the data communicating and saving on the computer will introduce a dead time of  $\sim 8$  s. We then post-process tens to hundreds of such saved and coherent-averaged interferograms with phase calibration, and thus obtain a single interferogram by averaging the phase-corrected interferograms. This post processing is referred to as “offline averaging” in this work. In the following calculation of the time-normalized optical SNR and the figure of merit of our dual comb spectrometer, only the effective data acquisition time is taken into account for the offline averaging, excluding the dead time.

## 7. SYSTEM'S SIZE AND PERFORMANCE

**System's size** — In our laboratory setup, the pumping source consists of two 3HU rack sized fiber laser combs, with an external box of fiber amplifiers (ca. 1HU and half rack sized). The photonic supercontinuum process is in a photonic chip base waveguide with the length of only 5mm, and the photonic chip coupling stage (including two 3-axis positioning stages) occupies a space of ca. 2HU and half rack size.

Although the system may have a large volume at the moment due to the free space coupling setup and the mode-locked laser module we used, it can be further reduced in size by means of engineering in the packaging, e.g. the packaging of photonic chips (directly with fiber coupling), and by using compact fiber laser sources. Significantly for the latter, there are now supercompact erbium fiber laser combs commercially available (e.g. the Menlo ELMO module), which combined with a packaged photonic chip ( $< 1$  cm<sup>-1</sup> in size) can form a miniature mid-IR dual-comb spectrometer capable of in-field applications.

As a comparison, a laboratory Fourier transform infrared spectroscopy (FTIR), with the same purpose of reaching sub-Doppler resolution (i.e.  $\mathcal{O}(100$  MHz), close to the mode spacing

of the optical frequency comb), can be much larger in size since a large optical path difference (in meter's level) unit is included.

**Gas detection sensitivity** — Taking the measurement in Fig. 3 (panel b) as an example, the gas detection sensitivity can be estimated as the following. When the gas concentration for CH<sub>4</sub> is 136.4 ppm in a 1.04-m long gas cell, a strong resonant absorption signal was measured at 3085.88 cm<sup>-1</sup>, peak absorbance 0.77. The standard deviation of the residual was calculated to be 0.0253 (in the region 2900~3150 cm<sup>-1</sup>). Thus, the signal-to-noise ratio (SNR) of the gas absorbance is calculated as  $0.77/0.0253 = 30.43$ , which is at the acquisition time of 52 s. Hence, the normalized and noise limited detection sensitivity is:  $136.4 \times 1.04 / (30.43 / \sqrt{52}) = 33.62$  ppm  $\cdot$  m/ $\sqrt{\text{Hz}}$ . Similarly, C<sub>2</sub>H<sub>2</sub> (concentration 406.5 ppm, peak absorbance 1.06 at 3304.97 cm<sup>-1</sup>, standard deviation of the residual 0.0288) has the sensitivity of 82.82 ppm  $\cdot$  m/ $\sqrt{\text{Hz}}$ .

Usually, the detection sensitivity is wavelength dependent and varies among gas samples, as the absorbance signal is different from mode to mode. Moreover, the level of sensitivity is highly related to the SNR of absorbance, which is mostly determined by the optical comb power. In our system, the mid-IR comb power in each beam is 1—3 mW, which is sufficient for spectroscopy but not powerful enough to support a higher sensitivity than the current level. Therefore, our detection sensitivity is only moderate compared with the best performance of dual-comb spectroscopy [4] or FTIR [5], which can achieve ppb-level sensitivity with maximum averaged comb power above 1 W. Nevertheless, there are also efforts in reducing the noise level while keep using low mid-IR comb power for spectroscopy, e.g. applying the feed forward scheme [6]. In this way, the SNR of absorbance can also be enhanced to support a high detection sensitivity.

**Optical signal-to-noise ratio and figure of merit** — To estimate the optical SNR of our dual-comb spectrometer, we took a dual-comb spectrum without gas samples (i.e. when the gas cell was purged), see Fig.S5(a), which is also the reference spectrum for the measurement in Fig. 3(a). We selected nine wavenumber positions that are distributed over the spectrum (indicated by vertical red dashed lines in Fig.S5(a)). At each wavelength a data section that contains 500 to 1000 data points is picked, for which the gas absorption (e.g. the water absorption) are always avoided. We next fitted the data with a sum-of-multiple-sine function. This step is to remove the oscillatory spectral background induced by the weak etalon effect in the system. The optical SNR at the selected position is then calculated as  $\frac{1}{\sigma}$ , where  $\sigma$  indicates the standard deviation (std.) of the normalized fitting residuals. As an example, at the position of 3205 cm<sup>-1</sup>, std. of residuals as a function of the averaging time, is displayed in Fig.S5(b, c). For long averaging time over 0.26 s, the offline averaging is applied. The averaged optical SNR as a function of the averaging time is presented in Fig.S5(d). The dependence of SNR on the averaging time (i.e. the normalized optical SNR) is extracted to be  $10/\sqrt{s}$ . Significantly, the offline averaging process is in consistent with the realtime coherent averaging, showing that the system remains stable during the dead time such that the data traces, after post correction on the phase drift, can fully contribute to reduce the white noise of the system. Therefore, our results demonstrate the effectiveness of coherent averaging process, and more importantly, the effectiveness of the offline averaging scheme that could largely extend system's performance, e.g. probing the short noise limit of the

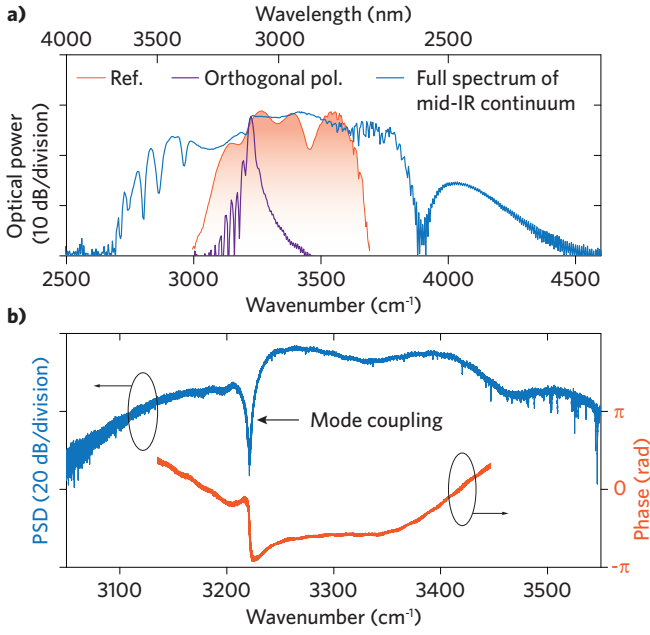


**Fig. S6. Mid-IR dual-comb spectroscopy on mode coupling induced resonant absorption.** (a) Spectral overlap between the mid-IR supercontinuum in the dual-core waveguide (blue curve, the spectrum is filtered out by the edge filter cut on at 2500 nm) and a referenced mid-IR comb as the dispersive wave generated in a conventional single-core waveguide (red curve), via the supercontinuum process pumped also at the telecom band. The generated orthogonal polarized wavelet is also presented (purple curve). (b) Retrieved intensity (blue curve) and the phase (red curve) information with respect to the mode coupling between the anti-symmetric TE mode and a high-order orthogonal polarized TM mode.

spectrometer.

In general, the figure of merit to characterize the performance of a dual comb spectrometer (i.e. the quality of the spectrum as well as the interferogram) is known as the quality factor<sup>[7]</sup>, which is the product of both the number of the comb elements ( $M$ ) and the optical SNR (at 1 s), namely  $Q = M \times SNR / \sqrt{t}$ . For our system, the averaged and normalized optical SNR is  $> 10 / \sqrt{s}$  (the peak SNR is  $\sim 25 / \sqrt{s}$ ), and the number of comb elements is  $> 1,000,000$ . Hence, the quality factor of our dual comb spectrometer is  $> 10^6 / \sqrt{s}$ .

## 8. MID-IR DUAL-COMB SPECTROSCOPY ON MODE COUPLING INDUCED RESONANT ABSORPTION

Resonant absorption is defined as the absorption of electromagnetic energy at a frequency such that the photon energy is equal to a quantum excitation energy of the absorbing system, which includes e.g. materials' band-gap absorption or molecular intrinsic vibrational absorption. In the case of pulse propagation in optical waveguides, the presence of a weak mode coupling (in which the source wave is assumed undepleted) would lead to a performance similar to the resonant absorption, and results in a Lorentzian resonance when there is phase matching between the coupled modes. In this context, the phase matching indicates that the momentum of the source wave is equal to a momentum that can excite a wave in the second mode. In our dual-core waveguides, the coupling of modes in different polarization directions satisfies the weak coupling condition, implying the existence of a resonant absorption at the phase matching wavelength of 3100 nm.

By means of the mid-IR dual-comb spectroscopy, we can ex-

perimentally detect this resonant absorption, see Fig. S6. In the measurement, we first prepared a mid-IR referenced comb, which is generated using a conventional single-core waveguide, by means of the mid-IR dispersive wave generation in the supercontinuum process, and is free of the mode coupling effect. The referenced comb is then set to be horizontally polarized, and covers the region of the mode coupling in the dual-core waveguide, see Fig. S6(a). In this way, the interference between the referenced comb and the mid-IR supercontinuum would feature a complete resonance lineshape with respect to the mode coupling, including both the intensity and the phase information. Moreover, from the linewidth of the resonance, one can extract the coupling strength as:

$$\kappa = |\beta_1(\omega_{3dB}) - \beta_2(\omega_{3dB})| \quad (S14)$$

where  $\omega_{3dB}$  indicates the angular frequency position where the absorption intensity is reduced by half (i.e. the 3-dB frequency position).

As a result, the retrieved absorption of the mode coupling is demonstrated to have a typical Lorentzian lineshape, in particular having the Lorentzian phase profile, namely a resonant absorption, see Fig. S6(b), and the coupling strength is measured to be on the level of  $1 \text{ mm}^{-1}$ .

## REFERENCES

1. H. Guo, X. Zeng, and M. Bache, "Generalized nonlinear wave equation in frequency domain," arXiv:13011473 (2013).
2. N. Akhmediev and M. Karlsson, "Cherenkov radiation emitted by solitons in optical fibers," *Phys. Rev. A* **51**, 2602 (1995).
3. K. L. Corwin, N. R. Newbury, J. M. Dudley, S. Coen, S. A. Diddams, K. Weber, and R. Windeler, "Fundamental noise limitations to supercontinuum generation in microstructure fiber," *Phys. Rev. Lett.* **90**, 113904 (2003).
4. A. Muraviev, V. Smolski, Z. Loparo, and K. Vodopyanov, "Massively parallel sensing of trace molecules and their isotopologues with broadband subharmonic mid-infrared frequency combs," *Nat. Photon.* **12**, 209 (2018).
5. F. Adler, P. Masłowski, A. Foltynowicz, K. C. Cossel, T. C. Briles, I. Hartl, and J. Ye, "Mid-infrared fourier transform spectroscopy with a broadband frequency comb," *Opt. Express* **18**, 21861–21872 (2010). Publisher: Optical Society of America.
6. Z. Chen, T. W. Hänsch, and N. Picqué, "Mid-infrared feed-forward dual-comb spectroscopy," *Proc. Natl. Acad. Sci.* **116**, 3454–3459 (2019).
7. I. Coddington, N. Newbury, and W. Swann, "Dual-comb spectroscopy," *Optica*, **3**, 414–426 (2016).